Electronic Supplementary Information

for

Effect of Post-synthesis Processing on the Electrochemical Performance of $Y_2W_3O_{12}$

Uttam Mittal[1,*], Matthew Teusner[1], Helen E. A. Brand[2], Jitendra Mata[3], Dipan Kundu[4], Neeraj Sharma[1]

[1] School of Chemistry, UNSW Sydney, Kensington, NSW 2052, Australia

[2] Australian Synchrotron, ANSTO, 800 Blackburn Rd., Clayton, Victoria 3168, Australia

[3] Australian Centre for Neutron Scattering, Australian Nuclear Science and Technology Organisation, Lucas Heights NSW 2234, Australia

[4] School of Chemical Engineering and Mechanical & Manufacturing Engineering, UNSW Sydney, Kensington 2052, Australia

* Corresponding author: uttam.mittal@unsw.edu.au

Table S1. Select publications on use of ceramic materials as anodes in lithium-ion batteries. For a more exhaustive list of ceramic electrode materials, please refer to Table 1 in a review by Sturman et al.[1]

Composition	Battery Performance	Reference
$Nb_{16}W_5O_{55}$	148 mAh/g at 3.43 A/g (20C)	Griffith et al.[2]
$Nb_{18}W_{16}O_{93}$	150 mAh/g at 2.98 A/g (20C)	Griffith et al.[2]
$NiNb_2O_6$	244 mAh/g at 118.1 mA/g (0.5C), 140 mAh/g at 2.36 A/g (10C), 50 mAh/g at 23.6 A/g (100C)	Xia et al.[3]
Sn/SiOCN	320 mAh/g at 2.22 A/g	Wang et al.[4]
$Sc_2Mo_3O_{12}$	150 mAh/g after 100 cycles at 17 mA/g	Liu et al.[5]
$Sc_2W_3O_{12}$	100 mAh/g after 100 cycles at 17 mA/g	Liu et al.[5]
$Al_2Mo_3O_{12}$	136 mAh/g after 100 cycles at 30 mA/g	Schulz et al.[6]
$Al_2W_3O_{12}$	96 mAh/g after 100 cycles at 30 mA/g	Schulz et al.[6]
WO_3/C hybrid	833.4 mAh/g after 100 cycles at 100 mA/g, 574.1 mAh/g after 100 cycles at 300 mA/g 528.3 mAh/g after 1300 cycles at 500 mA/g	Xiao et al.[7]
Pure WO_3	460.3 mAh/g after 100 cycles at 100 mA/g	Xiao et al.[7]

Table S2. The table comparing the size of Y^{3+} in octahedral coordination vs the other trivalent cations.[8]

Trivalent Cation	Ionic Radius in Octahedral Coordination (Å)
Y^{3+}	0.9
Sc^{3+}	0.745
Al^{3+}	0.535
Cr^{3+}	0.615
Fe^{3+}	0.645
Ho^{3+}	0.901
Er^{3+}	0.89
Tm^{3+}	0.88
Yb^{3+}	0.868
Lu^{3+}	0.861

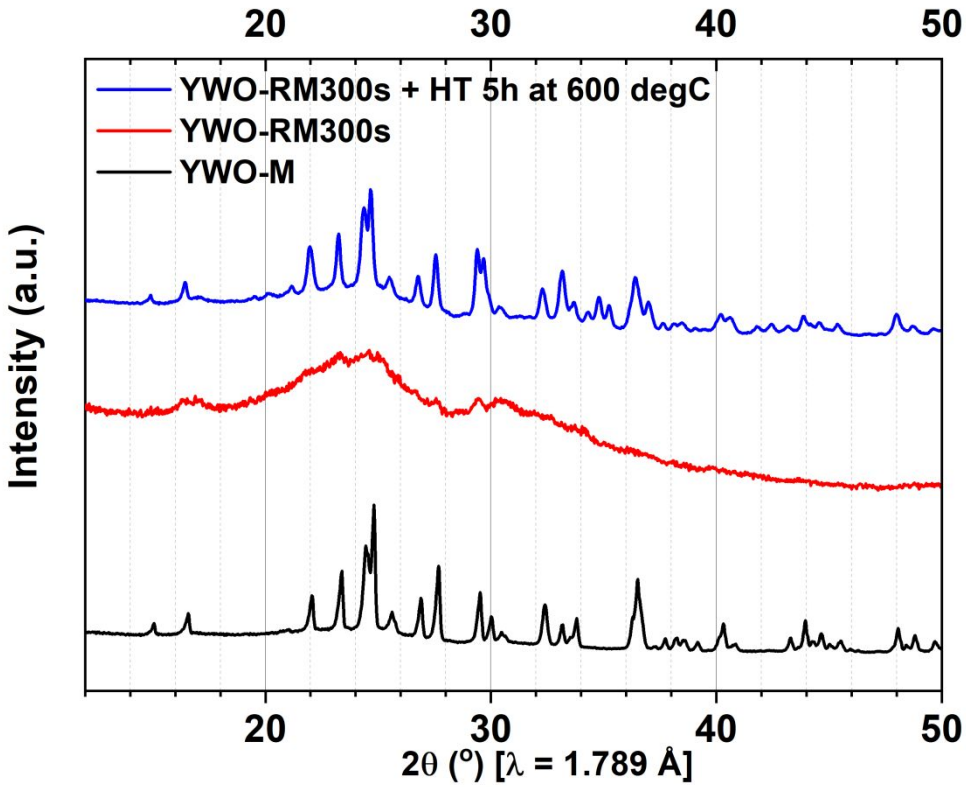

Figure S1. XRD patterns for YWO-M, YWO-RM300s, and YWO-RM300s after the heat treatment at 600 °C for 5 h in air. The re-appearance of distinct and sharp peaks in YWO-RM300s after the heat treatment at 600 °C suggests the coalescence of nanosized particles into larger crystalline domains.

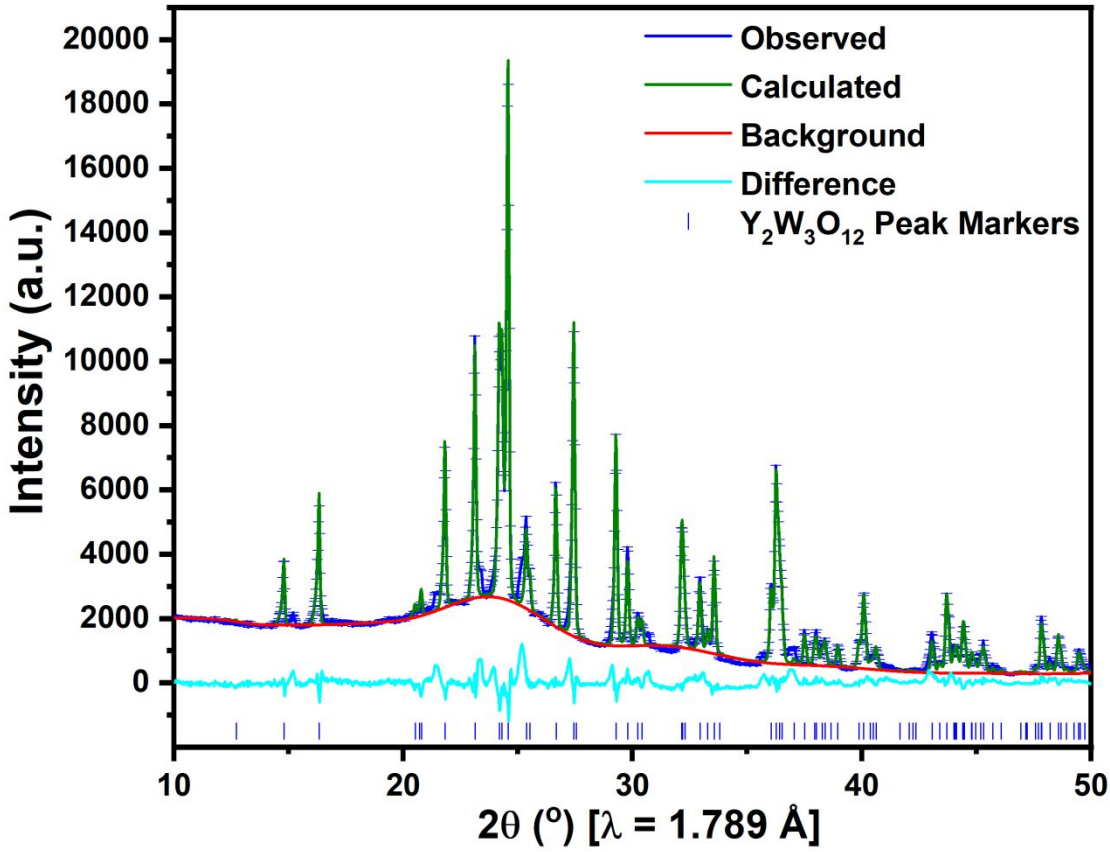

Figure S2. Rietveld-refined structural model of CCYWO-M with XRD data. The observed data are represented in blue; the calculated model is shown in green, the difference between the observed data and the model is shown in cyan, the background is shown in red, and the peak markers representing the Bragg reflections for $Y_2W_3O_{12}$ are shown in blue. (*a = 10.0782(3) Å, b = 13.9508(4) Å, c = 9.9865(3) Å; and unit cell volume (V) = 1404.10(5) Å^3, Space Group: Pnca, No. of refined parameters = 47, R_{wp} = 10.8%)*

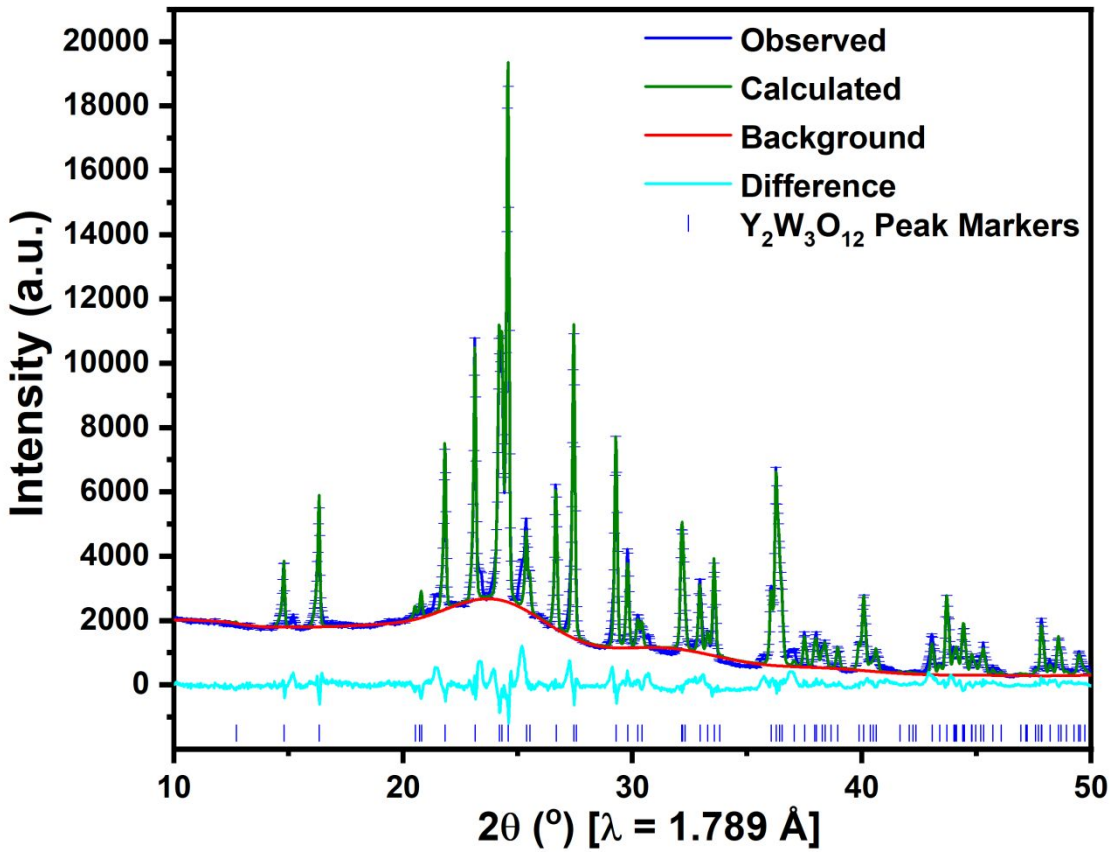

Figure S3. Rietveld-refined structural model of CCYWO-RM300s with XRD data. The observed data are represented in blue; the calculated model is shown in green, the difference between the observed data and the model is shown in cyan, the background is shown in red, and the peak markers representing the Bragg reflections for $Y_2W_3O_{12}$ are shown in blue. (*a = 10.0731(7) Å, b = 13.9568(11) Å, c = 9.9865(8) Å; and unit cell volume (V) = 1404.0(2) Å^3, Space Group: Pnca, No. of refined parameters = 47, R_{wp} = 11.9%)*

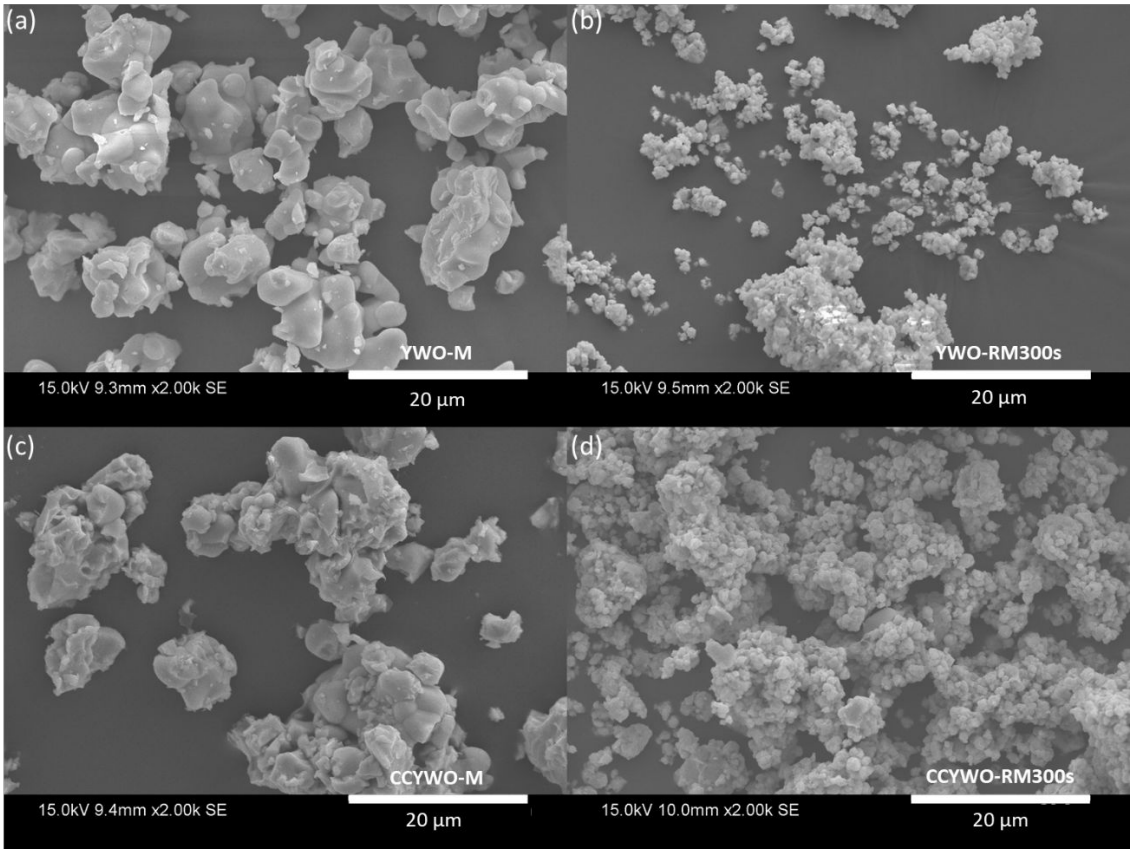

Figure S4. SEM images for (a) YWO-M, (b) YWO-RM300s, (c) CCYWO-M, and (d) CCYWO-RM300 showing the morphological changes among the samples.

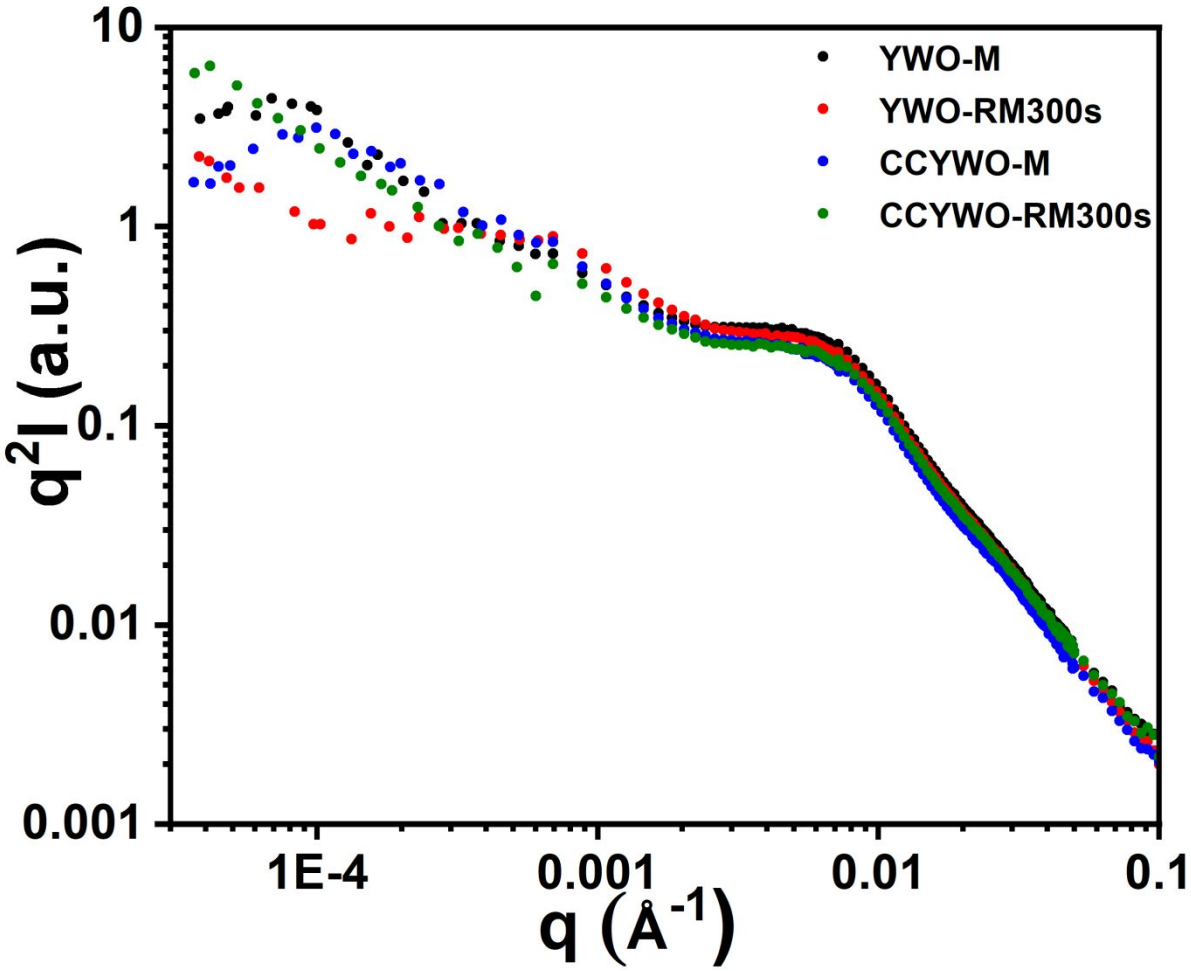

Figure S5. Kratky plots (q^2I vs q) of the USANS/SANS data for the as pristine electrodes. The data on the axes are plotted on the logarithmic scale.

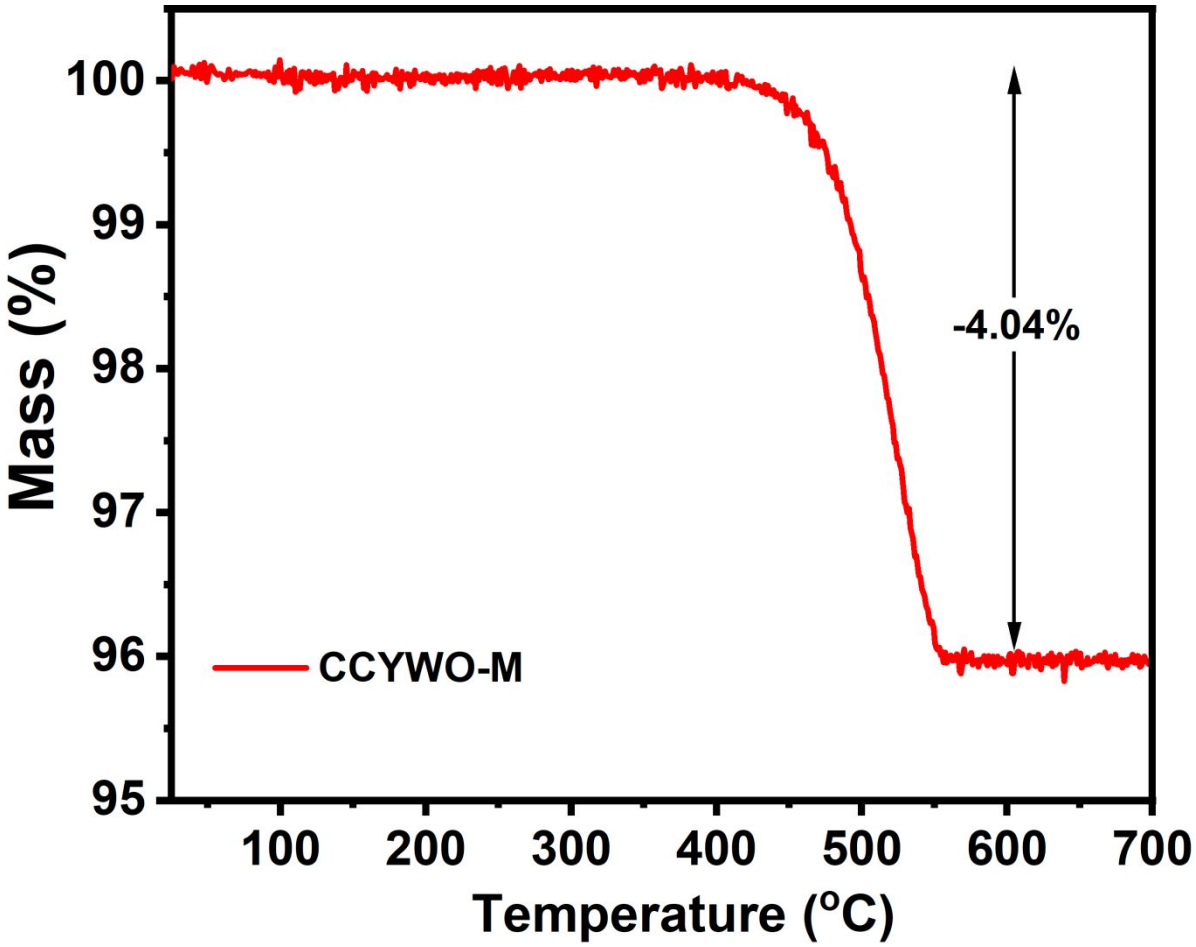

Figure S6. TGA analysis on the carbon coated CCYWO-M sample to assess the weight fraction of the carbon layer encapsulating the YWO-M particles.

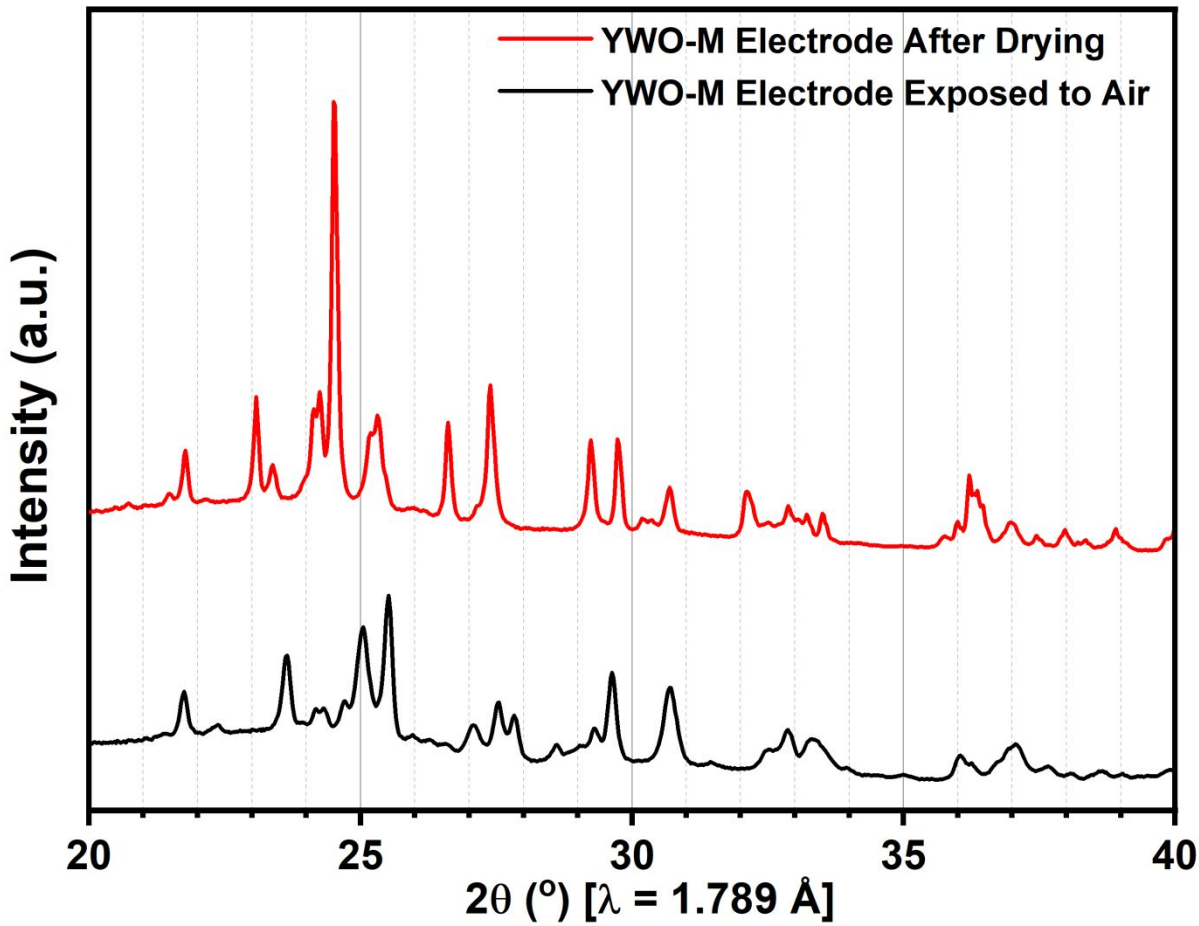

Figure S7. XRD pattern of the electrode before and after the drying step to illustrate the change in structure due to moisture uptake.

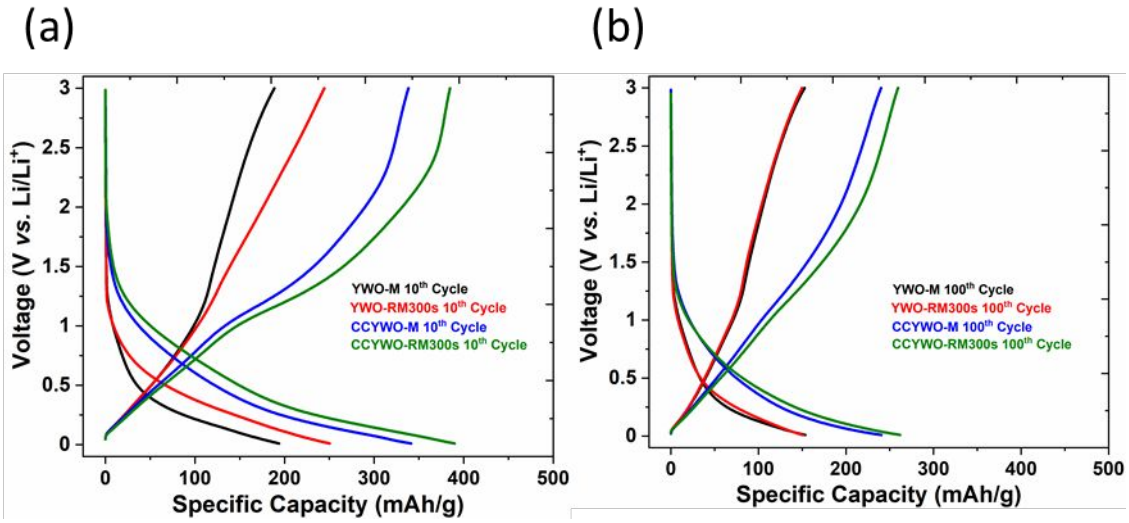

Figure S8. Comparison of Galvanostatic (dis)charge voltage-capacity profiles during (a) 10th and (b) 100th cycles for YWO-M, YWO-RM300s, CCYWO-M, and CCYWO-RM300s electrodes cycled between 0.01 and 3.0 V at a current density of 100 mA/g.

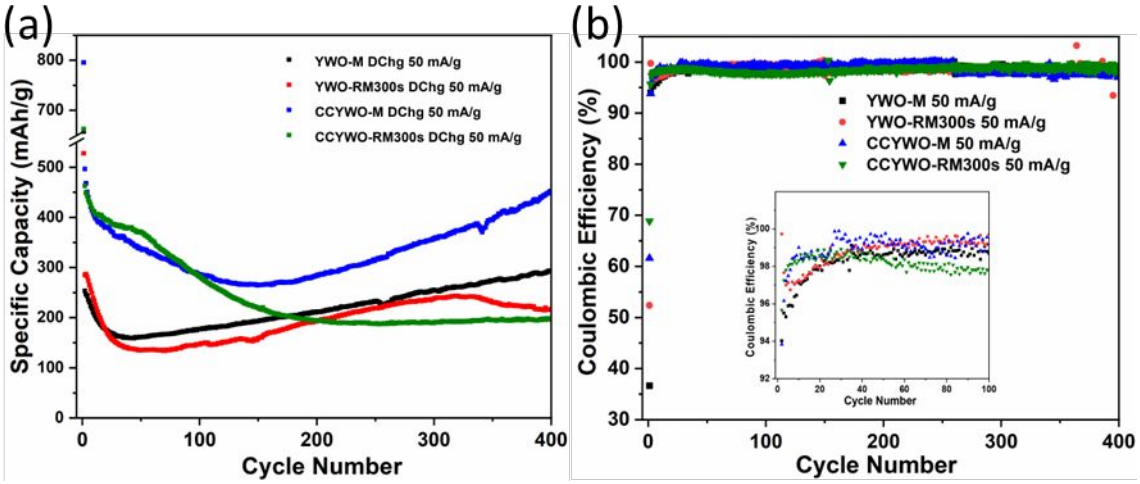

Figure S9. The comparison of electrochemical performance of the cells with YWO-M, YWO-RM300s, CCYWO-M, and CCYWO-RM300s electrodes cycled between 0.01 and 3.0 V. (a, b) Long-term specific discharge (lithiation) capacity obtained during the galvanostatic cycling at 50 mA/g and the corresponding Coulombic efficiencies. The insets in (b) highlights the differences in CE in the initial stages of cycling.

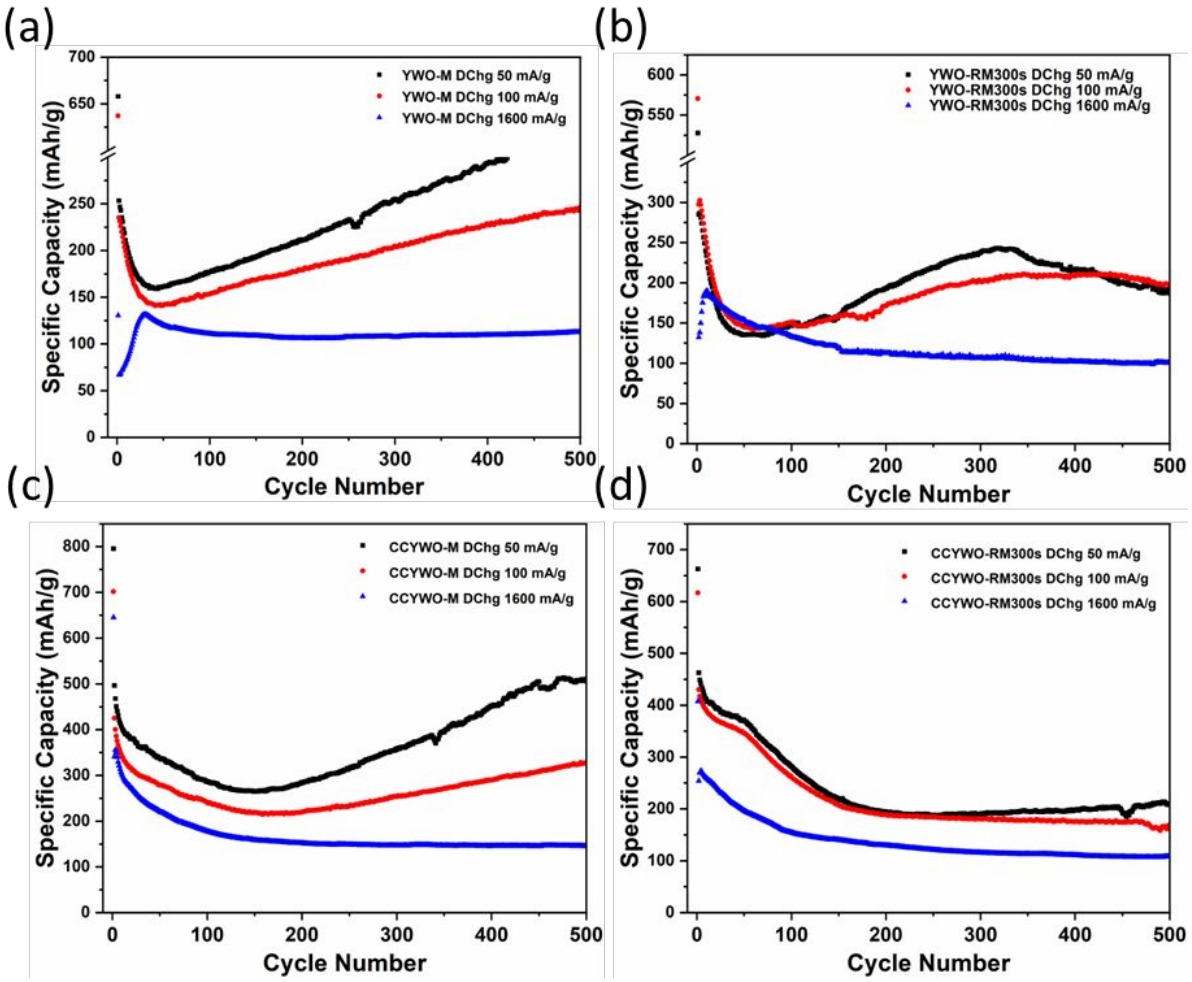

Figure S10. Long-term cycling performance comparison based on the discharge capacities at current densities of 50, 100, and 1600 mA/g for (a) YWO-M, (b) YWO-RM300s, (c) CCYWO-M, and (d) CCYWO-RM300s.

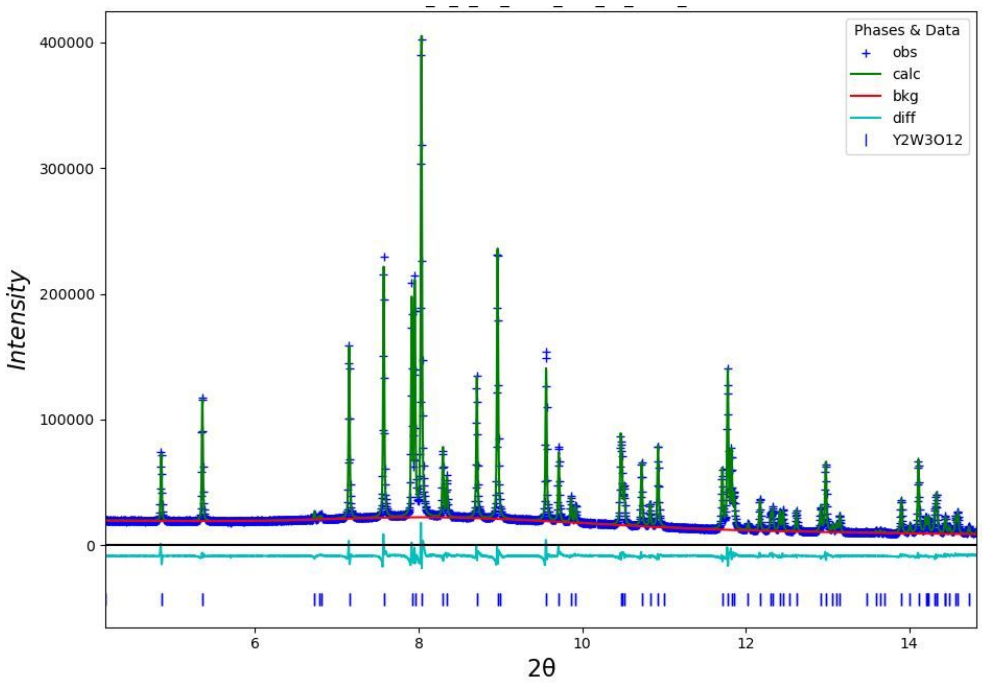

Figure S11. Rietveld refinements of the structural model with *ex situ* synchrotron data obtained for the 0% Li discharged in YWO-M sample collected at 100 °C using the *Pnca* model of $Y_2W_3O_{12}$, λ = 0.59063(3) Å, Rwp = 3.8%.

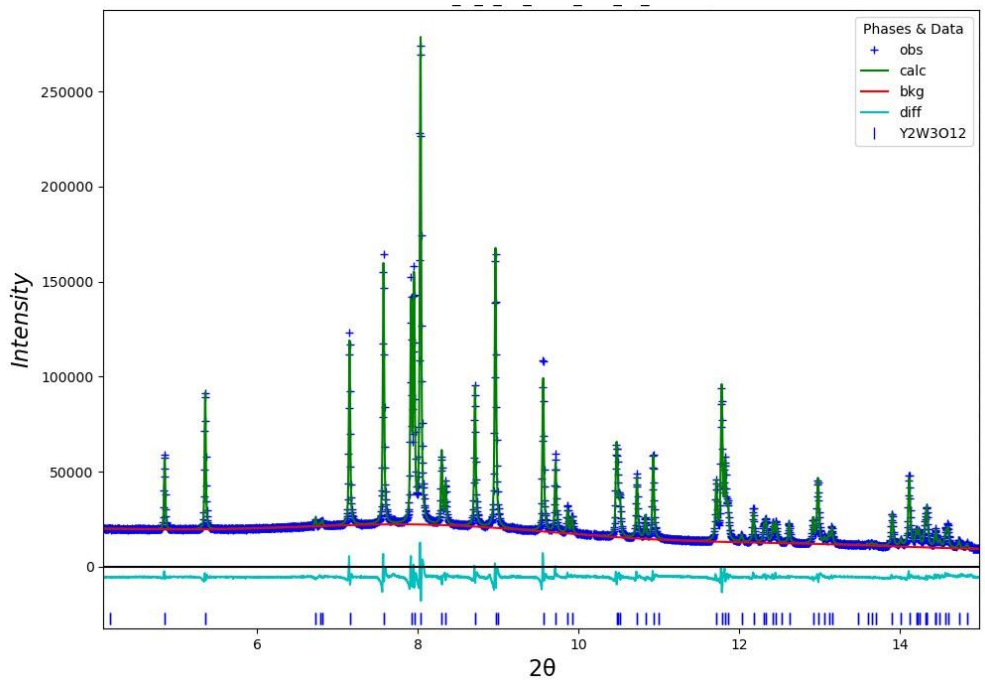

Figure S12. Rietveld refinements of the structural model with *ex situ* synchrotron data obtained for the 5% Li discharged in YWO-M sample collected at 100 °C using the *Pnca* model of $Y_2W_3O_{12}$, λ = 0.59063(3) Å, Rwp = 3.41%.

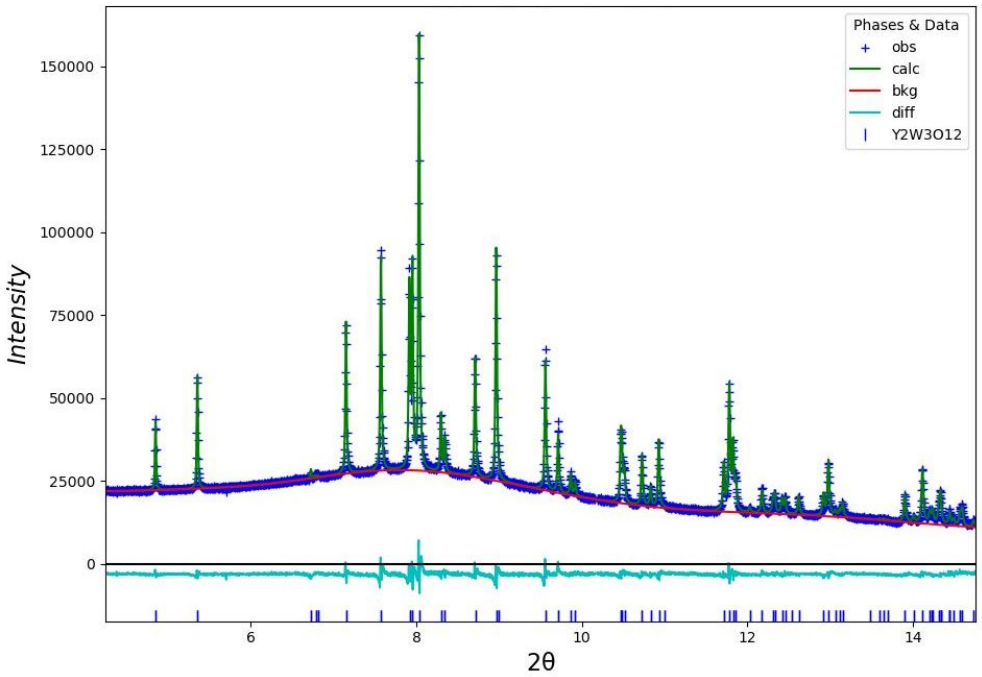

Figure S13. Rietveld refinements of the structural model with *ex situ* synchrotron data obtained for the 12.5% Li discharged in YWO-M sample collected at 100 °C using the *Pnca* model of $Y_2W_3O_{12}$, λ = 0.59063(3) Å, Rwp = 2.23%.

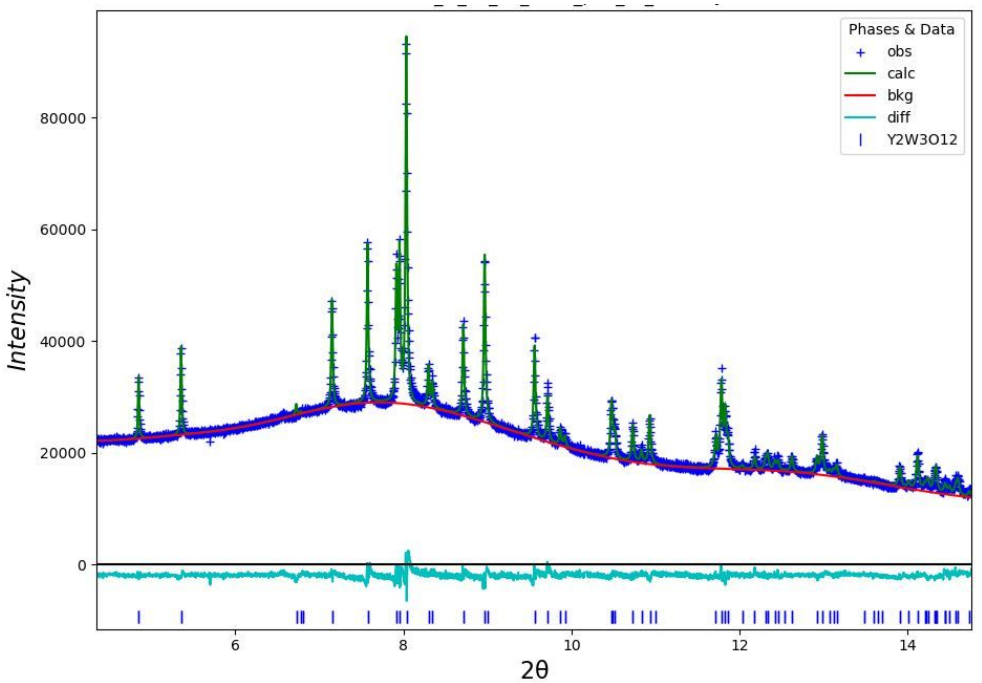

Figure S14. Rietveld refinements of the structural model with *ex situ* synchrotron data obtained for the 25% Li discharged in YWO-M sample collected at 100 °C using the *Pnca* model of $Y_2W_3O_{12}$, λ = 0.59063(3) Å, Rwp = 1.99%.

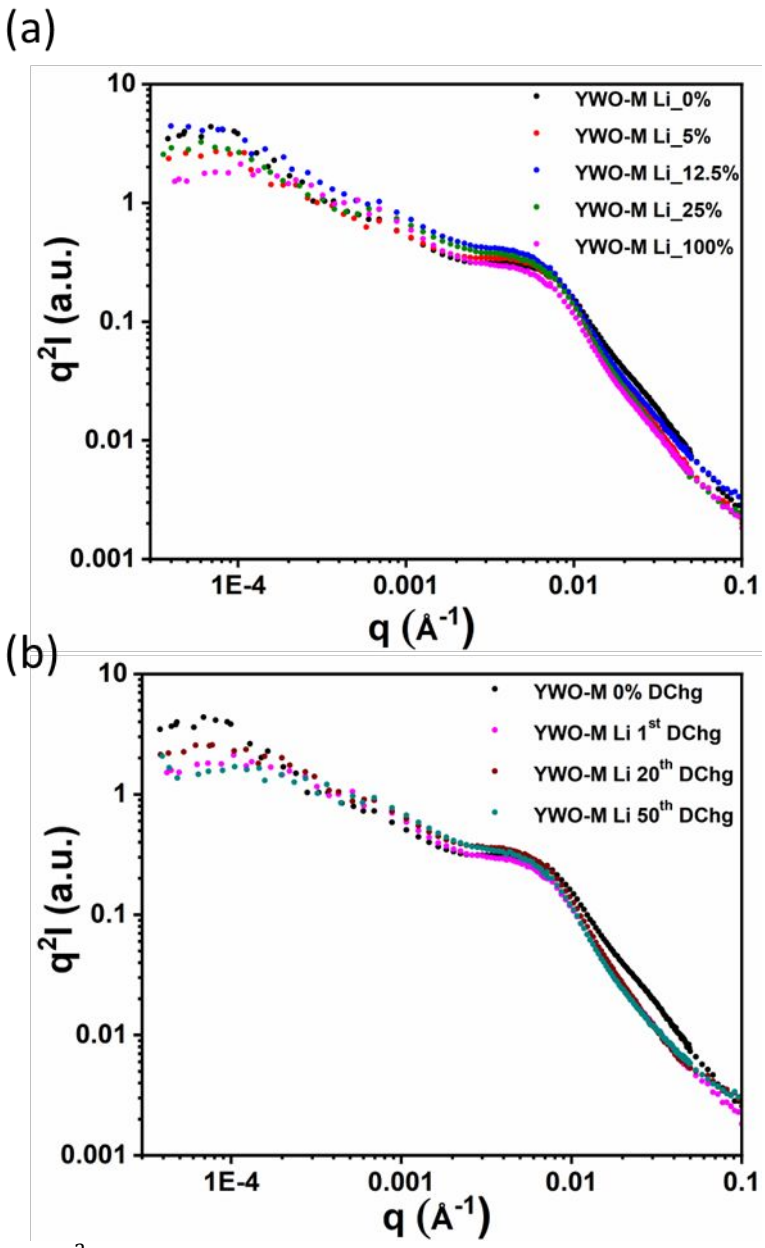

Figure S15. Kratky plots (q^2I vs q) of the USANS/SANS data for the (a) YWO-M electrodes with different levels of Li-insertion during 1st discharge, and (b) on electrodes recovered after 1st. 20th, and 50th discharge. The data on the axes are plotted on the logarithmic scale.

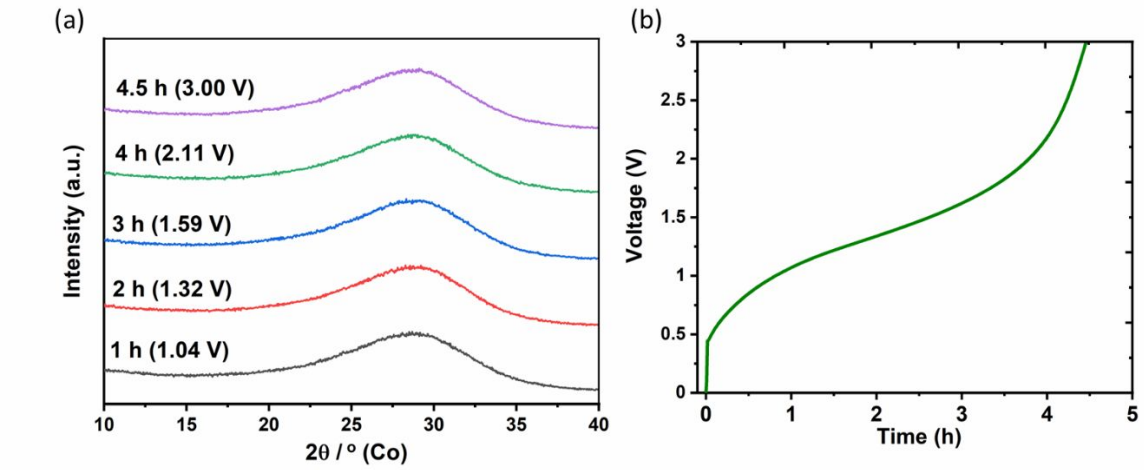

Figure S16. (a) *Operando* XRD patterns for YWO-M anode during 1st charge at 50 mA/g. The 1st charge delivered a capacity of 227 mAh/g. It is clear from the trend in the patterns that there is no structural reversibility observed during the charging. (b) The voltage-time profile for the 1st charge.

References:

(1) Sturman, J. W.; Baranova, E. A.; Abu-Lebdeh, Y. Review: High-Entropy Materials for Lithium-Ion Battery Electrodes. *Front. Energy Res.* **2022**, *10*. https://doi.org/10.3389/fenrg.2022.862551.

(2) Griffith, K. J.; Wiaderek, K. M.; Cibin, G.; Marbella, L. E.; Grey, C. P. Niobium Tungsten Oxides for High-Rate Lithium-Ion Energy Storage. *Nature* **2018**, *559* (7715), 556–563. https://doi.org/10.1038/s41586-018-0347-0.

(3) Xia, R.; Zhao, K.; Kuo, L.; Zhang, L.; Cunha, D. M.; Wang, Y.; Huang, S.; Zheng, J.; Boukamp, B.; Kaghazchi, P.; Sun, C.; ten Elshof, J. E.; Huijben, M. Nickel Niobate Anodes for High Rate Lithium-Ion Batteries. *Adv. Energy Mater.* **2022**, *12* (1), 2102972. https://doi.org/10.1002/aenm.202102972.

(4) Wang, J.; Kober, D.; Shao, G.; Epping, J. D.; Görke, O.; Li, S.; Gurlo, A.; Bekheet, M. F. Stable Anodes for Lithium-Ion Batteries Based on Tin-Containing Silicon Oxycarbonitride Ceramic Nanocomposites. *Mater. Today Energy* **2022**, *26*, 100989. https://doi.org/10.1016/j.mtener.2022.100989.

(5) Liu, J.; Johannessen, B.; Brand, H. E. A.; Andersen, H. L.; Sharma, N. The Sc 2 W x Mo 3−x O 12 Series as Electrodes in Alkali-Ion Batteries. *CrystEngComm* **2021**, *23* (21), 3880–3891. https://doi.org/10.1039/D1CE00318F.

(6) Schulz, B.; Andersen, H. L.; Al Bahri, O. K.; Johannessen, B.; Liu, J.; Primig, S.; Sharma, N. Electrochemical Performance and Structure of Al 2 W 3−x Mo x O 12. *CrystEngComm* **2018**, *20* (10), 1352–1360. https://doi.org/10.1039/C7CE01707C.

(7) Xiao, Y.; Jiang, M.; Cao, M. Developing WO3 as High-Performance Anode Material for Lithium-Ion Batteries. *Mater. Lett.* **2021**, *285*, 129129. https://doi.org/10.1016/j.matlet.2020.129129.

(8) Shannon Radii http://abulafia.mt.ic.ac.uk/shannon/ptable.php (accessed Jan 18, 2023).